Heterogeneous Metasurface Empowering Proximate High-Permittivity Ceramic Cover for a 5G Dual-Band Millimeter-Wave Smartphone

Byeongjin Kim, *Graduate Student Member, IEEE*, Jaebaek Jung, *Graduate Student Member, IEEE*,
Sumin Yun, Hosaeng Kim, *Member, IEEE*, and Jungsuek Oh, *Senior Member, IEEE*

Abstract— This study presents a heterogeneous metasurface that facilitates the close integration of a high-permittivity ceramic back cover into a 5G dual-band millimeter-wave (mmWave) smartphone. The metasurface can be applied to various types of target antennas without additional modification to the antenna design. Furthermore, the proposed metasurface technology is significant because it enables the active use of ceramic covers in 5G mmWave smartphones. Despite its many design and practical advantages, the ceramic cover could not be applied in 5G mmWave smartphones, because of its high reflection loss in the FR2 bands. A transmissive metasurface that eliminates this high reflection loss and further improves the antenna performance is designed at an extremely close distance to the antenna-in-package (AiP). A heterogeneous unit cell grouping topology is proposed to achieve dual-bandwidth control and wide bandwidth. The influence of the distance between the metasurface and AiP is investigated to determine near-field compatibility and design compactness. Five distinct antenna arrays, including a commercial AiP embedded in a 5G smartphone, are simulated with and without metasurfaces, and an effective isotropically radiated power (EIRP) and cumulative distribution function (CDF) is measured using the mobile call test, including the AiP and metasurface-attached ceramic cover, to verify gain, and beam coverage enhancement.

Index Terms— 5G, antenna-in-package (AiP), dual-band, metasurface, millimeter-wave (mmWave), smartphone.

I. Introduction

RECENTLY, the commercialization of 5G millimeter-wave (mmWave) devices and many mmWave antennas have been investigated [1], [2], [3], [4], [5], [6], [7], [8], [9]. In particular, 5G mmWave smartphones with low-profile form

factors have been developed by embedding compact antenna-in-package (AiP) modules [1], [2], [3], [4], [5], [6] on the back panel and bezel. During this process, major manufacturing companies have continued adopting glass materials for the back cover to pack the AiPs along with the motherboard. For example, glass products are often utilized [10], [11]. Although they have fair hardness, the major disadvantage of a glass cover is that, when it breaks, the internal panel is often damaged as well, resulting in high repair costs. The glass–ceramic type has also been adopted in some products to improve hardness.

Ceramics have many fascinating advantages in terms of design and practicality; therefore, they have been adopted in some LTE and Sub-6 GHz 5G smartphones [12]. For example, they have a stunning metallic luster that is not present in glass. Moreover, they are harder than glass, enabling bezel-less displays in some LTE smartphones, such as Xiaomi's Mi MIX. Additionally, they exhibit high scratch and heat resistances. They can protect the internal panel by absorbing shock when damaged because they crumble into small pieces owing to its relatively low toughness. They also have low RF loss.

Despite the numerous advantages of ceramic covers, they cannot be adopted for 5G mmWave smartphones. Commercial ceramics have a high permittivity above 10, resulting in a high reflection loss when placed close to 5G mmWave AiP modules. Notably, the distance between the back cover and AiP of modern smartphones is shorter than 1 mm because of their low-profiled form factors. Consequently, the impedance matching, array antenna gain, and beam coverage of mmWave AiP are significantly deteriorated.

The mmWave AiPs in glass-back-covered smartphones are optimized by considering the proximity of their glass covers. However, optimization of AiPs with ceramic back covers is relatively difficult because of their high permittivity. An alternative solution that saves design time and cost to embed a metasurface between the back cover and AiPs. This method can eliminate reflection loss without redesigning the AiPs. Such reflection-eliminating metasurfaces have been proposed for both far- [13], [14], [15], [16], [16], and near-field environments [17] for glass covers. In particular, [17] proposed a single-band wideband grid-shaped metasurface attached to a glass cover operating in n257 and n258 bands (24.25–29.5 GHz). 5G transmissive metasurfaces closely inte-

grated with the antennas have been reported [18], [19], [20]. However, housing covers have not been considered for these metasurface-integrated antennas. Moreover, these metasurfaces significantly affect the bandwidths of the antennas, and the antennas cannot properly radiate without a metasurface.

In this study, a heterogeneous dual-band metasurface that enables the proximate integration of a ceramic back cover for a 5G mmWave smartphone is proposed. In Section II, design constraints, such as the frequency and form factor of the AiP and metasurfaces are explained by presenting and investigating single-band metasurfaces. Section III describes a novel metasurface design technique for grouping heterogeneous unit cells for dual-band bandwidth control. The designed metasurface with and without this technique was applied to the exemplified patch arrays and a commercial AiP module with different frequency bands and polarizations in Section IV. Section V presents the conclusion.

The key contributions of this article compared to previous studies including [17] can be summarized as follows.

1) The issue this article aims to tackle diverges significantly from the one presented in [17]. In [17], the objective was to devise a single-band metasurface suitable for the typical glass cover with a dielectric constant of 6.69, aimed at mitigating minimal reflection losses. In contrast, our paper proposes a dual-band metasurface tailored for ceramic covers with a dielectric constant of 30, a material previously unexplored in 5G mmWave smartphones due to its high reflection loss.

2) In this article, the approach to interpreting the ultra-near-field scenario differs significantly from that proposed in [17]. It is shown that beyond a minimum distance between the antenna and metasurface, Floquet port impedances can be simply set to be air impedance. This insight challenges the design method explained in [17].

3) This article proposes a topology of heterogeneous unit cell grouping to achieve dual-bandwidth control and wide bandwidth. The proposed design includes the grouping of subunit cells with different sizes and periods, significantly widening the bandwidth of the higher frequency band.

II. DESIGN CONSTRAINTS OF THE NEAR-FIELD CERAMIC COVER METASURFACE WITH THE MMWAVE AIP

A. Predetermined Design Constraints

The target frequency bands of the proposed dual-band metasurface were n261 and n260 (27.5–28.35 and 37–40 GHz), which are widely available 5G mmWave bands in the United States. The predetermined form factors of the components, including AiP and the back cover in a commercial 5G mmWave smartphone (Samsung Galaxy S22+), are shown in Fig. 1. The lateral dimension of the prototype antenna arrays for the dual-band metasurface was determined to be 3.5×23.5 mm, which was directly measured from commercial AiP modules embedded in the target smartphone. The back cover and air gap have thicknesses of 0.59 and 0.764 mm, respectively. The metasurface should be embedded in the air gap rather than
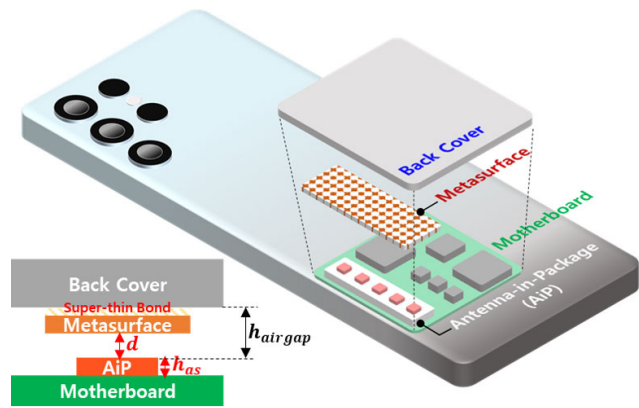

Fig. 1. Demonstration of the proposed scheme of integrating near-field dual-band metasurface in the air gap between the back-cover and the motherboard.
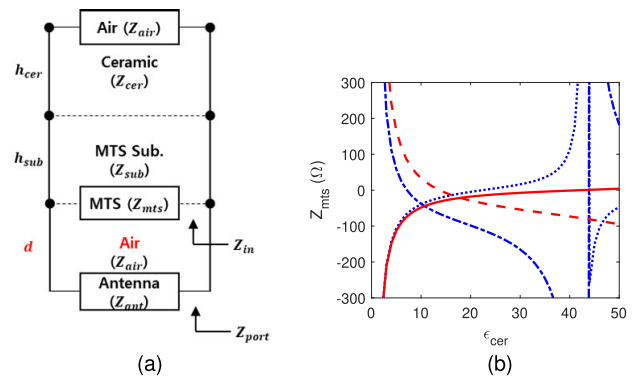

Fig. 2. (a) Equivalent circuit model of a ceramic cover, a metasurface substrate (MTS Sub.), a single-layered metasurface, and an antenna. (b) Calculated $Z_{mts} = R + jX$ versus ceramic permittivity ϵ_{cer} (red solid and dashed line R and X at 28 GHz, blue dotted and dash-dotted line R and X at 38.5 GHz).

outside the cover to be protected from the environment. Therefore, the metasurface is placed at an extremely close distance to the AiP, i.e., approximately 0.764 mm or less, which is less than 0.070 λ_0 at the lowest frequency. It should be noted that the metasurface was affixed to the ceramic using an optically clear adhesive (OCA), which is a super-thin adhesive film with a thickness of 25 μm and a dielectric constant of 2.58. As OCA had little impact on metasurface and antenna performance, it is omitted in the following figures and text for the sake of simplicity and readability.

B. Maximum Thickness of the Metasurface

The harsh distance condition was tested for a single mmWave frequency band, before proceeding to the design of dual-band metasurface. Fig. 2(a) shows the equivalent circuit model for a single-metal-layered metasurface and antenna. The ceramic and metasurface substrate used for the cover material had dielectric constants of 30 and 2.2 and loss tangents of 0.004 and 0.003, respectively. From basic calculations, $Z_{cer} = 68.8\Omega$, $Z_{sub} = 254.2\Omega$, and $Z_{air} = 377\Omega$. The thicknesses were predetermined as $h_{cer} = 0.59$ mm and $h_{airgap} = 0.764$ mm, and h_{sub} was set to the appropriate thickness of 0.127 mm. To eliminate the reflection loss caused by a ceramic cover, Z_{port} with and without the ceramic-metasurface
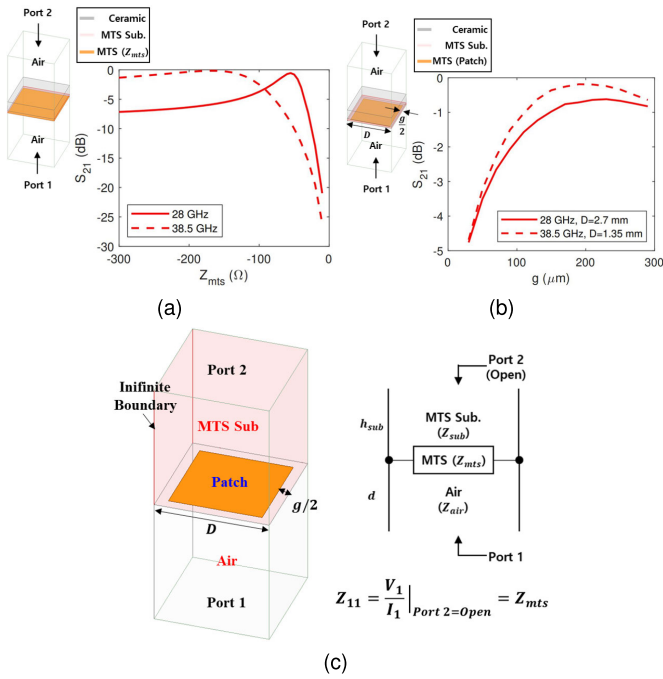
Fig. 3. Transmittance of a ceramic cover with single-band metasurface (CCM), (a) with Z_{mts} and (b) with the patch element. (c) Simulation setup for deriving g and D from Z_{mts}.
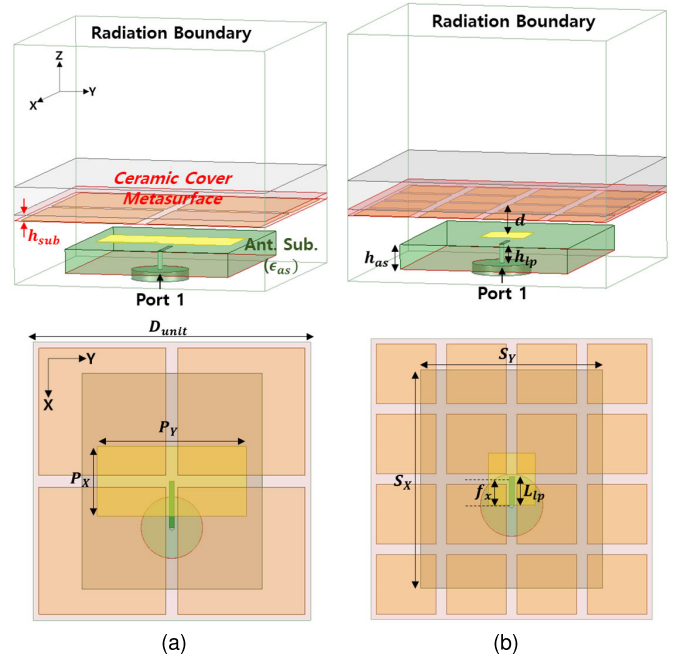

Fig. 4. Simulated L-probe patch antenna with ceramic cover metasurface (CCM) and infinite boundary condition. $(D_{unit}, S_X, S_Y, h_{as}, h_{lp}) =$(5.4, 4.2, 3.5, 0.508, 0.127), and (P_X, P_Y, f_X, L_{lp}) is equal to (a) (1.35, 2.9, 0.9, 0.9) for 28 GHz, (b) (1, 0.9, 0.5, 0.55) for 38.5 GHz (unit: mm), $\epsilon_{as} = 10.2$.

composite must be identical, i.e., $Z_{in} = Z_{air}$. Accordingly, if a single-layer metal pattern is placed under the substrate, its impedance Z_{mts} is calculated to be $-7.4 - j53.9$ and $16.3 - j165.0$ Ω, respectively, for the 28 and 38.5 GHz antennas. The real and imaginary components of Z_{mts} based on the dielectric constant of ceramic, ϵ_{cer}, are shown in Fig. 2(b). An advantage of ceramics with the predetermined thickness is that, owing to their high permittivity, the real components of Z_{mts} are removed, rendering the design procedure significantly easy.

The transmittance of a ceramic cover with metasurface (CCM) based on the Z_{mts} values was simulated using HFSS with an infinite boundary condition, as shown in Fig. 3(a). The reflection loss is minimized with the previously calculated Z_{mts} values, as expected from the equivalent circuit model. The negative-imaginary-component-dominant Z_{mts} implies an equivalent capacitance in the circuit model. Therefore, the single-layered metal pattern of the metasurface can be modeled as a periodic patch array with a unit cell period D and a gap between patches g, as shown in Fig. 3(b). D and g were selected by using a two-port Floquet unit cell simulation, as shown in Fig. 3(c). This method is most precise when the thickness of the metasurface substrate is infinite. Since the thickness is limited, an optimization procedure for the final selection of D and g is necessary to minimize the transmission loss for the ceramic-metasurface integrated unit cell. D at 28 and 38.5 GHz were predetermined to be 2.7 and 1.35 mm, respectively, for a common period when the antenna unit cell simulation is conducted (Fig. 4). The g values for two single-band metasurfaces were determined as 0.23 and 0.2 mm, respectively, for 28 and 38.5 GHz.
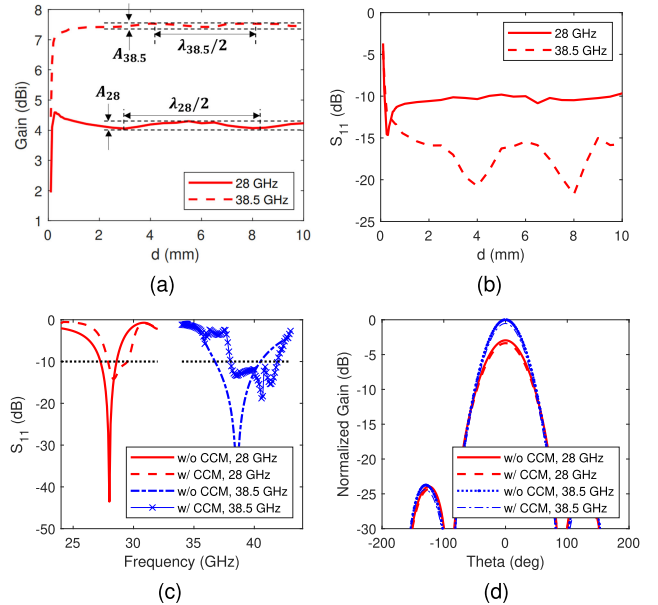

Fig. 5. Simulated results of L-probe patch antenna with ceramic cover metasurface and infinite boundary condition. (a) Gain and (b) S_{11} with the variation of d. In case that $d = 0.637$ mm $(h_{airgap} = 0.764$ mm). (c) S_{11} and (d) the E-plane element patterns with and without CCM at 28 and 38.5 GHz.

The infinite boundary condition was also applied for the L-probe patch antennas with single-band metasurfaces, assuming an ideal infinite antenna array environment, as shown in Fig. 4. If the antenna element is significantly close to the metasurface, its impedance is affected by electromagnetic (EM) coupling. The distance d between the antenna and metasurface was varied in HFSS to assess electromagnetic coupling, while keeping the thickness of the metasurface, metasurface substrate (MTS sub.), and antenna substrate (Ant. sub.) fixed—only altering h_{airgap}, as shown in Fig. 5. In this manner, one
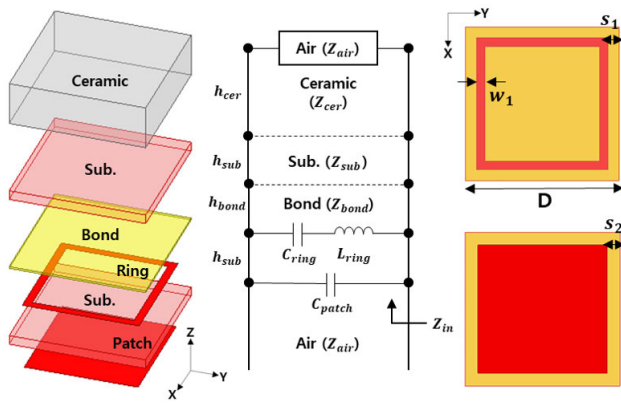
Fig. 6. Illustration of the dual-band SUC and its equivalent circuit model. $(h_{sub}, h_{bond}, D, w_1, s_1, s_2)$=(0.127, 0.025, 1.8, 0.1, 0.13, 0.15) (unit: mm) and $(\epsilon_{sub}, \epsilon_{bond}, (tan\ \delta)_{sub}, (tan\ \delta)_{bond})$=(2.2, 3.9, 0.0009, 0.038).

Fig. 7. SUC transmittance with the variation of (a) D, (b) s_1, and (c) s_2.

Fig. 8. Illustration of (a) a grouped unit cell (GUC) composed of main unit cell (MUC) and AUC, and (b) AUC. $(D, D_a, w_1, s_{1a}, s_{2a})$ = (1.8, 1.1, 0.1, 0.17, 0.15) and parameters for MUC as SUC as follows (D, w_1, s_1, s_2)=(1.8, 0.1, 0.1, 0.15) (unit mm).

can observe the effects of EM coupling exclusively, while ensuring that the designed Z_{in} remains unchanged, maintaining a value akin to Z_{air}. Notably, if d increases from 0, the EM coupling decreases and the gain of the antenna with CCM increases. The gain saturates rapidly as d exceeds 0.270 and 0.315 mm, respectively at 28 and 38.5 GHz, and becomes greater than the gain without CCM (4.8 and 7.75 dBi at 28 and 38.5 GHz, respectively) minus 1 dB. Then, the gain fluctuates vertically within a 0.3 dB ripple (A_{28} and $A_{38.5}$) and with a half wavelength period (λ_{28} and $\lambda_{38.5}$), as shown in Fig. 5(a). This is because of the little impedance mismatch between Z_{in} and Z_{air}. This mismatch sinusoidally varies with a period of half the wavelength along a transmission line (air) in the equivalent circuit model shown in Fig. 2(a). Consequently, considering the constraint that h_{airgap} is fixed at 0.764 mm in reality, the maximum thickness of the dual-band metasurface is calculated to be $h_{airgap} - max(d_{min,28}, d_{min,38.5})$=0.449 mm.

Fig. 5(c) and (d) show that both the impedance bandwidths and element patterns were maintained despite the existence of the CCM at the near-field by comparing results with (w/) and without (w/o) CCM. Notably, the total frequency range within the bandwidth is shifted while including the target frequency. Because the transmission bandwidth of the CCM is limited, it operates as an impedance surface at other frequencies, affecting Z_{port}.

III. DESIGN PROCEDURE OF THE DUAL-BAND CERAMIC COVER METASURFACE

Fig. 6 shows a dual-band CCM unit cell comprising a stacked patch and ring and its equivalent circuit model, modeling the patch and the ring as C and a series LC [21], respectively. Herein, this unit cell type is termed a singular unit cell (SUC). s_1 and s_2 determine the first and second resonant frequencies, respectively, and D controls both resonant frequencies, as shown in Fig. 7. As a result, the optimal values for D, s_1, and s_2 were determined as 1.8, 0.13, and 0.15 mm, respectively, exhibiting dual-band -3 dB transmission bandwidth of 2.56 (26.40–28.96 GHz) and 2.55 GHz (37.19–39.74 GHz). Although the two resonant frequencies could be selected by adjusting the three variables, the bandwidth expansion of the high band to satisfy the n260
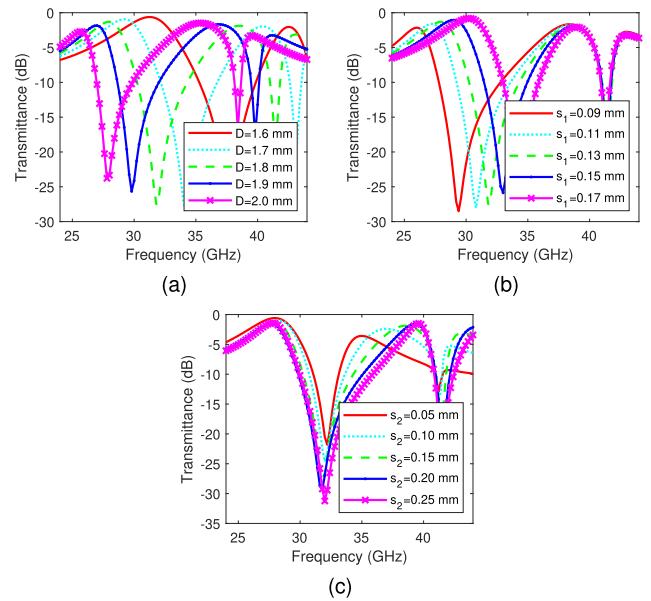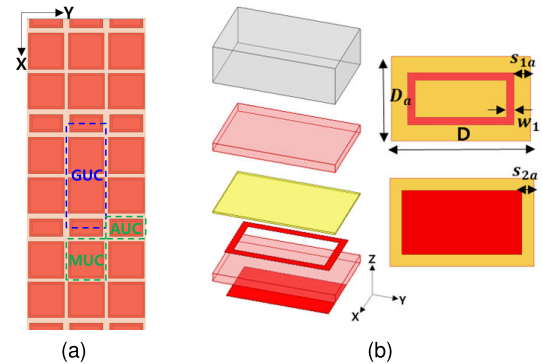
band (37–40 GHz) has a limitation. Notably, the proposed ring-patch unit cell is not the unique SUC solution for dual-band operation. However, despite numerous attempts to design optimal metal patterns satisfying at least -3 dB transmission bandwidth for both n261 and n260 5G mmWave bands (27.5–28.35 and 37–40 GHz), the SUC could not satisfy such a dual-bandwidth when the form factors were restricted as discussed in Section II. Therefore, we proposed a novel metasurface-designing method that groups heterogeneous unit cells into a subarray.

Fig. 8 shows a heterogeneous unit cell subarray comprising two main unit cells (MUCs) and one assistant unit cell (AUC) and its equivalent circuit model. This unit cell type is termed a grouped unit cell (GUC). The MUC is the same square-shaped ring-patch type unit cell as the SUC, but the AUC is rectangular-shaped to affect periodicity. In other words, the period of the MUC becomes nonuniform because of the existence of the AUC. Consequently, assuming $s_{1a} = s_1$ and $s_{2a} = s_2$, the bandwidth of the high band of the GUC varies as D_a varies, as shown in Fig. 9(a). D_a was set to
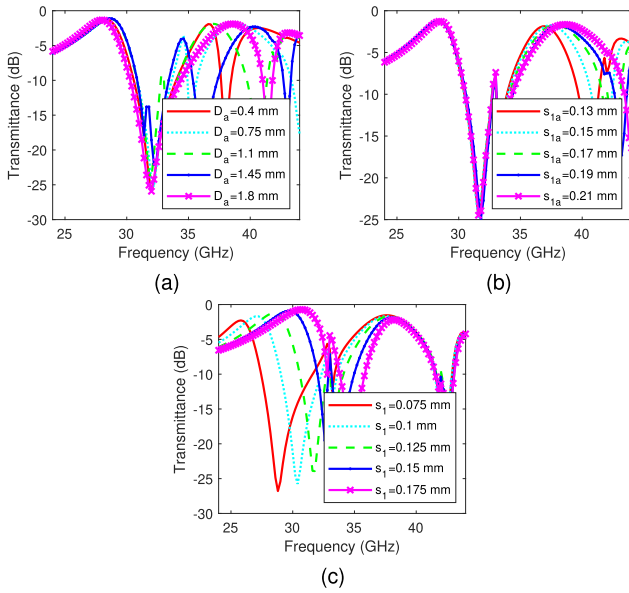
Fig. 9. GUC transmittance with X polarization with the variation of (a) D_a, (b) s_{1a}, and (c) s_1.
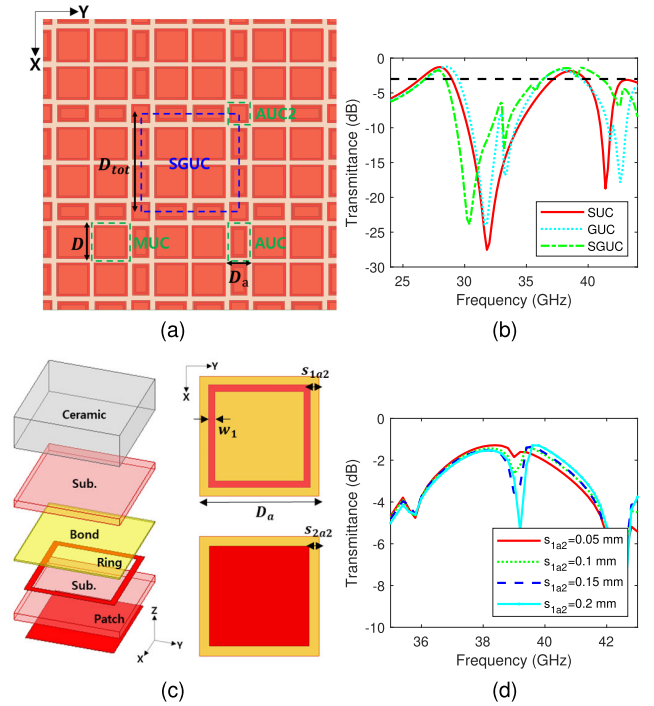

Fig. 10. (a) Illustration of the symmetrical GUC (SGUC). (b) Transmittance comparison between SUC, GUC, and SGUC. (c) Illustration of the secondary AUC (AUC2). (d) SGUC transmittance with the variation of s_{1a2}. The design parameters for the SGUC are as follows $(D_{tot}, D, D_a, w_1, s_1, s_2, s_{1a}, s_{2a}, s_{1a2}, s_{2a2})$=(4.7, 1.8, 1.1, 0.1, 0.15, 0.21, 0.15, 0.1, 0.15) (unit: mm).

1.1 mm to set the long dimension of GUC to 4.7 mm, which is equal to the previously determined array spacing. The periods of GUC and array antenna elements were synchronized to achieve maximum equalization of element patterns by equalizing an antenna-element-surrounding environment, for high array performance. Other MUC and AUC parameters were co-optimized, achieving 2.60 and 3.05 GHz -3 dB transmission bandwidths (26.86–29.46 and 36.38–39.43 GHz) for X polarization. s_{1a} is a crucial parameter to control the bandwidth of a high band after D_a is fixed. Notably, the first resonant frequency is fixed by selecting s_1, as shown in Fig. 9(b) and (c).

The symmetrical type of GUC (SGUC) is also designed to optimize both the low and high bands, enabling coverage of the entire n261 and n260 bands, as shown in Fig. 10. The SGUC exhibits 1.67 and 4.76 GHz -3 dB transmission bandwidths (26.78–28.45 and 36.36–41.12 GHz) for both polarizations, including the n261 and n260 bands, with sufficient margins. The SGUC exhibits a wider -3 dB transmittance bandwidth in the high band than the GUC due to the split in the band caused by the addition of the secondary AUC, as depicted in Fig. 10(b). The crucial design parameter of the secondary AUC is s_{1a2}. The bandwidth of the high band widens as s_{1a2} increases because it splits further. However, it eventually diminishes because the notch in the middle of the high band exceeds a 3 dB transmission loss, as shown in Fig. 10(d). The optimized values for s_{1a2} and s_{2a2} were determined to be 0.1 mm and 0.15 mm, respectively. Consequently, the bandwidth of the high band was extremely expanded, whereas that of the lower band was narrowed because the n260 bandwidth (3 GHz) is wider than the n261 bandwidth (0.85 GHz). Finally, three types of finite- and compact-sized metasurfaces were designed considering AiP integration, as shown in Fig. 11. Herein, metasurfaces composed of SUC, GUC, and SGUC, respectively, were termed as SMTS, GMTS, and SGMTS, respectively. SGMTS has the most compact configuration.
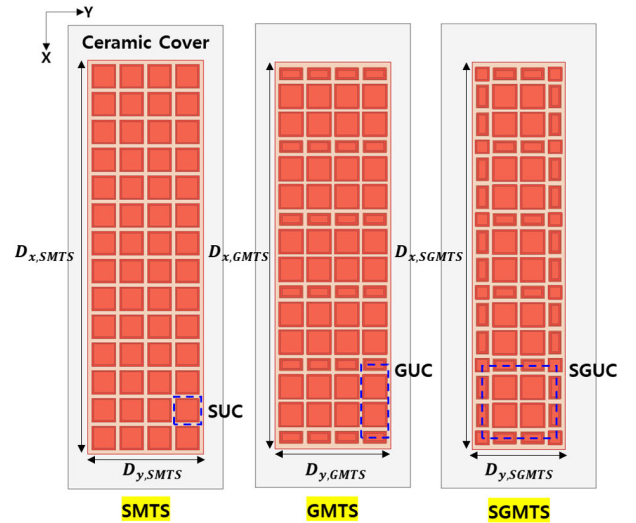

Fig. 11. Illustration of the metasurface prototypes each composed of SUC (SMTS), GUC (GMTS), and SGUC (SGMTS). Design parameters as follows $(D_{x,SMTS}, D_{x,GMTS}, D_{x,SGMTS})$=(25.5, 25, 25), and $(D_{y,SMTS}, D_{y,GMTS}, D_{y,SGMTS})$=(7.5, 7.5, 6) (unit: mm).

IV. CERAMIC COVER METASURFACE AND AiP INTEGRATION: EXPERIMENTAL RESULTS

A. Simulation Results With 3 GHz Bandwidth AiPs

To verify the effects of the proposed proximate metasurfaces and compare the performances of the three metasurfaces (SMTS, GMTS, and SGMTS), four five-element antenna arrays with 3 GHz bandwidths were designed, as shown in
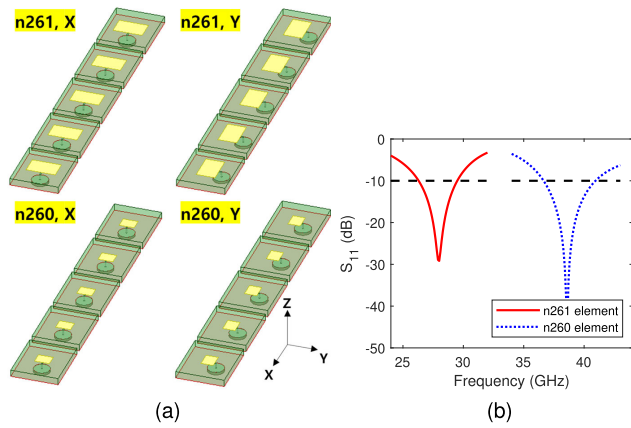
Fig. 12. (a) Four five-element antenna arrays with L-probe patch antenna design parameters demonstrated in Fig. 4 as follows $(S_X, S_Y, P_X, P_Y, f_x, L_{lp})$=(4.2, 3.5, 1.35, 2.1, 0.8, 0.7) for the n261 arrays and (4.2, 3.5, 0.88, 1.1, 0.45, 0.4) for the n260 arrays (unit mm). (b) S_{11} curves for n261 and n260 elements, respectively.
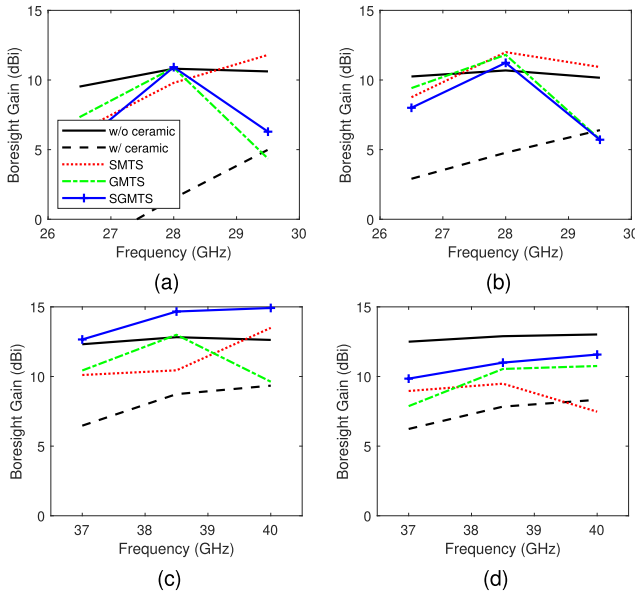

Fig. 13. Simulated boresight gain of array antennas with and without the ceramic cover, SMTS, GMTS, and SGMTS. (a) (n261, X) array, (b) (n261, Y) array, (c) (n260, X) array, and (d) (n260, Y) array.

Fig. 12. Each L-probe patch array has center frequencies and polarizations of 28 and 38.5 GHz and X and Y polarizations. They have a common lateral dimension of 3.5 mm × 23.5 mm, as discussed in Section II.

Fig. 13 shows the simulated boresight gain of the four antenna arrays with and without the ceramic cover, SMTS, GMTS, and SGMTS, at 26.5, 28, 29.5, 37, 38.5, and 40 GHz. Although 26.5 and 29.5 GHz are not included in the n261 band, these frequencies were included to observe the correlation between the metasurface transmission responses and the gain enhancement of array antennas. As a result, because limits were imposed in the transmission bandwidths of the three metasurfaces, gain enhancement in the low frequency band was only achieved at 28 GHz. Moreover, SGMTS exhibited the best gain enhancement in all bands and polarizations, except for the n261 band with Y polarization. However, it still enhances the gain of the (n261, Y) array.
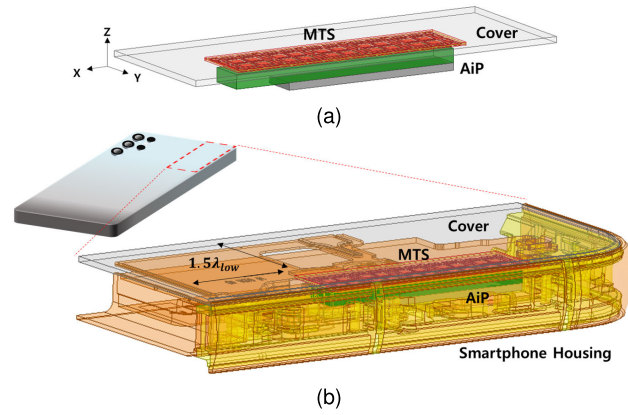

Fig. 14. Simulation models for the commercial AiP and metasurfaces (a) without and (b) with the smartphone housing.

Notably, SGMTS exhibits a higher gain increase for the X-polarized array compared to the Y-polarized array. This discrepancy arises from the unequal number of SGUCs in the X- and Y-axis directions. Furthermore, SGMTS exhibits superior gain enhancement magnitude and bandwidth at every frequency point in the n260 band compared with SMTS and GMTS, which are attributed to its: 1) widest transmission bandwidth in the n260 band (4.76 GHz) and 2) synchronized period of the GUC with that of array antennas. Therefore, the proposed design topology, which groups heterogeneous unit cells into a subarray, is verified to be effective in controlling and improving the gain-bandwidth of a target antenna with the designed metasurface. Notably, SGMTS is also the smallest metasurface among the three metasurfaces.

B. Simulation Results With Commercial 5G mmWave AiP

To verify the applicability of the designed metasurfaces for various types of antennas without further design modifications, an encrypted HFSS file of an AiP module that is embedded in a 5G mmWave smartphone (Samsung Galaxy S22+) was used for the simulation. Without any knowledge of the antenna design, two kinds of simulations were conducted. First, the 5G AiPs without the smartphone housing were tested, as shown in Fig. 14(a). Second, the 5G AiPs with the smartphone housing were tested, as shown in Fig. 14(b). An HFSS file of the smartphone housing was also provided by the company. The file reflected approximate shape and material property information for the components surrounding the AiP.

Fig. 15 shows the simulated boresight gain of the commercial AiP with and without a ceramic or glass cover and the metasurfaces. For both n261 and n260 bands, SGMTS and GMTS exhibited an enhanced gain over commercialized products (glass covers) and ceramic covers for most of the frequencies and polarizations, regardless of the existence of smartphone housing. Notably, the results with and without the smartphone housing exhibited different gains because of the complicated effects of surface waves, reflection, and scattering resulting from the large housing surrounding the AiP. The beam-scanned radiation patterns of an AiP with an integrated smartphone housing and X polarization, are shown in Fig. 16. The superior magnitudes of the beam scan envelope of the
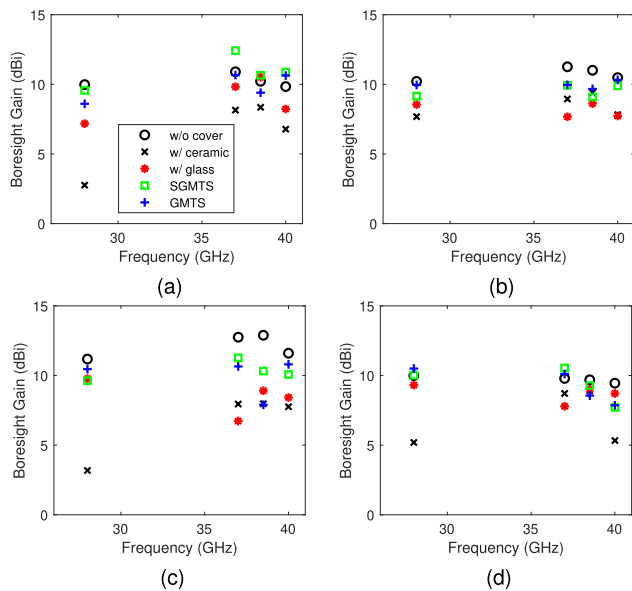
Fig. 15. Simulated boresight gain of a commercial AiP embedded in 5G smartphone with and without the ceramic or glass cover, SMTS, GMTS, and SGMTS: (a) *X* and (b) *Y* polarization without smartphone housing, and (c) *X* and (d) *Y* polarization with smartphone housing.
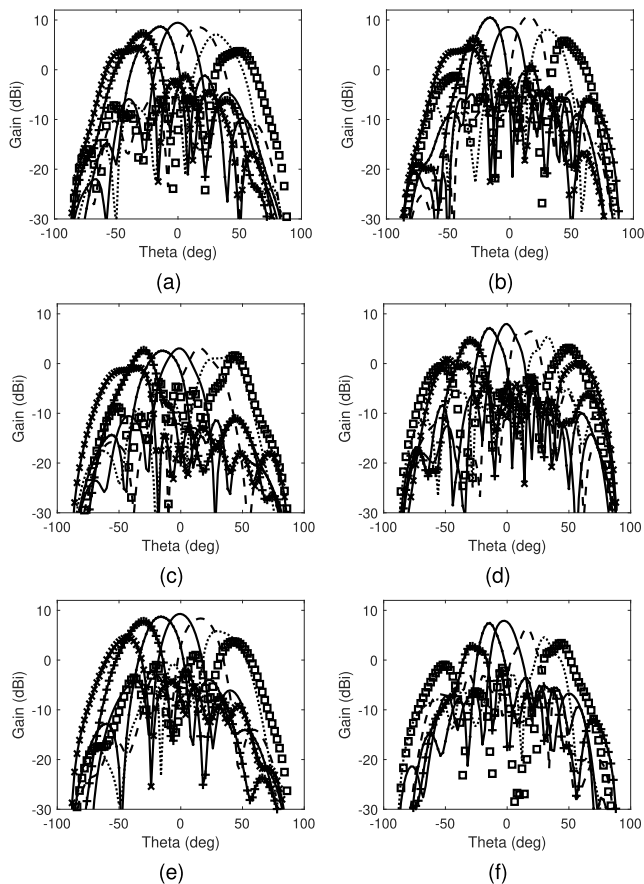

Fig. 16. Simulated beam scanned radiation patterns of a commercial AiP with SGMTS or covers and smartphone housing integrated, with *X* polarization (a) 28 and (b) 38.5 GHz with SGMTS, (c) 28 and (d) 38.5 GHz with a ceramic cover, and (e) 28 and (f) 38.5 GHz with a glass cover.

SGMTS in mmWave dual-bands than ceramic and glass covers indicate that the spherical beam coverages were also improved by integrating the proposed metasurface.
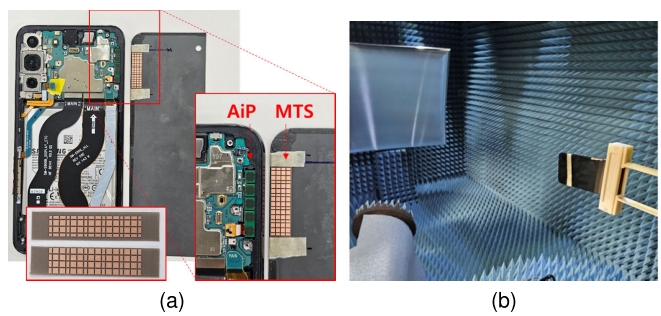

Fig. 17. (a) Sample photograph of 5G AiP and CCMs (GMTS and SGMTS) with a 5G mmWave Smartphone. (b) Measurement setup in compact antenna test range (CATR) anechoic chamber.
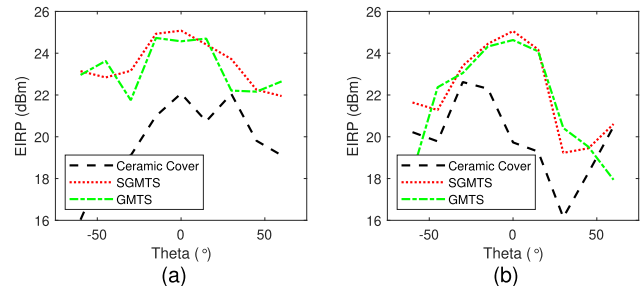

Fig. 18. Measured EIRP of 5G Aip integrated with smartphone housing and metasurfaces at different angles. (a) 28 GHz and (b) 38.5 GHz. Input power to the five channels (corresponding to five elements) of the AiP is 16 dBm.

C. Fabrication and Measurement Results With Commercial 5G mmWave AiP Embedded in the Smartphone Housing

The GMTS and SGMTS were embedded in a 5G mmWave smartphone (Samsung Galaxy S22+) above the commercial AiP, which is connected to a motherboard and battery, with a specially fabricated ceramic cover, as shown in Fig. 17(a). To supply power to the AiP and scan the radiated beam, the AiP was embedded in the smartphone housing. As radiation patterns are distorted by this smartphone housing, measuring an effective isotropically radiated power (EIRP) and cumulative distribution function (CDF) for the entire spherical domain was effective in evaluating the gain and beam coverage enhancing ability of the CCM-integrated commercial 5G mmWave AiP, rather than measuring radiation patterns in several planes. The EIRP was measured at the compact antenna test range (CATR) anechoic mmWave chamber located in Samsung, as shown in Fig. 17(b). In the measurement process, a call test was conducted using a small mmWave base station device. In other words, when a base station makes a call to a smartphone, the received power is measured through the receiving antenna in the chamber. The main beam of the 5G AiP was maximally steered at every rotational state of the 5G smartphone in the entire radiating sphere.

The maximum EIRPs of the AiP with and without a ceramic cover and metasurfaces at different beam-steered directions are shown in Fig. 18. The EIRPs with *X* and *Y* polarizations were root-mean-squared to calculate the total EIRP. SGMTS exhibits a better overall EIRP than the GMTS at 28 and 38.5 GHz. SGMTS and GMTS exhibited peak EIRPs of 25.08 and 24.73 dBm at 28 GHz, respectively, which are 3.01 and 2.66 dB larger than the 22.07 dBm of the
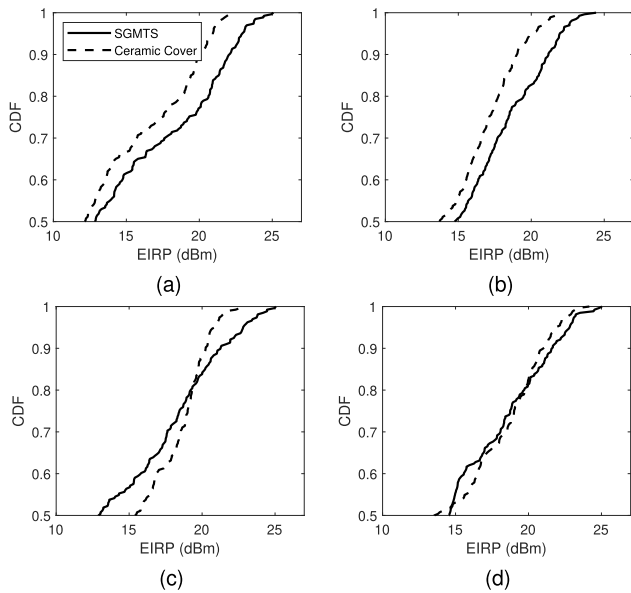
Fig. 19. Measured total EIRP CDF of 5G AiP with the ceramic cover and SGMTS. (a) 28 GHz, (b) 37 GHz, (c) 38.5 GHz, and (d) 40 GHz.

TABLE I
COMPARISON OF STATE-OF-THE-ART PROXIMATE METASURFACE-INTEGRATED 5G MMWAVE ANTENNAS

Ref.	Frequency (GHz)	MTS-antenna distance (λ_{low})	Purpose of MTS	Housing cover	Cover material (ϵ_r, $\tan\delta$)
[17]	23.5-32.2	0.060	Cover loss removal	Yes	Glass (6.69,0.013)
[18]	24-40	0.0024	Impedance matching	No	-
[19]	24.1-29.5	0.041	Impedance matching	No	-
This work	26.8-28.5, 36.4-41.1	0.038	Cover loss removal	Yes	Ceramic (30,0.004)

* λ_{low} is the free-space wavelength at the lowest frequency.

Table I shows the comparison of state-of-the-art proximate metasurface-integrated 5G mmWave antennas. In [18] and [19], proximate metasurfaces were embedded to improve impedance matching in wide bandwidth for antennas with narrow bandwidth. They aimed to achieve strong electromagnetic coupling between the antenna and metasurface to enhance antenna performance. Conversely, [17] and this article integrated the proximate metasurfaces to mitigate transmission loss induced by the housing covers, making these metasurfaces versatile and suitable for various types of already well-developed commercial AiPs. In contrast to [17], the proposed metasurfaces in this article are applicable to high-permittivity ceramic covers, which offer numerous practical and esthetic advantages over commonly used glass covers. Additionally, a novel analysis method enabled closer placement of the metasurface to the antenna. Lastly, a novel heterogeneous unit cell subarray grouping technique was proposed to achieve wide dual-bandwidth control.

ceramic cover. They also exhibited peak EIRPs of 25.06 and 24.63 dBm at 38.5 GHz, respectively, which are 2.44 and 2.01 dB larger than the 22.62 dBm of the ceramic cover. The distortion in the measured EIRP scan patterns and a slight difference with simulated results are caused by complicated EM coupling with the smartphone housing and metallic components that could not be perfectly reflected in the simulation. Nevertheless, the EIRPs of the metasurface-integrated cases tend to be larger than those of the ceramic-cover-integrated case, and their peak EIRPs are considerable to satisfy 5G requirements, as explained subsequently.

Fig. 19 shows the EIRP CDF of 5G AiP with the ceramic cover and SGMTS with the smartphone housing at the n261 and n260 bands (28, 37, 38.5, and 40 GHz). Smartphones are categorized as power class 3 (PC3) defined in the 3GPP specifications [22]. For PC3, the peak EIRP (CDF=1) must reach 22.4 and 20.6 dBm in the n261 and n260 bands, respectively. Moreover, the minimum EIRP (CDF=0.5) must reach 11.5 and 8 dBm in the n261 and n260 bands, respectively. The peak EIRP of 5G AiP is increased with SGMTS by 3.01 dB (22.07 to 25.08 dBm), 2.63 dB (21.81 to 24.44 dBm), 2.44 dB (22.62 to 25.06 dBm), and 0.87 dB (24.17 to 25.04 dBm), at 28, 37, 38.5, and 40 GHz, respectively. The minimum EIRP is also increased with SGMTS by 0.69 dB (12.16 to 12.85 dBm), 1.04 dB (13.71 to 14.75 dBm), and 1.02 dB (13.54 to 14.56 dBm) at 28, 37, and 40 GHz, respectively, except for 38.5 GHz, where the minimum EIRP is decreased by 2.52 dB (15.42 to 12.9 dBm). Nevertheless, the peak and minimum EIRPs were generally increased and satisfied the 3 GPP specifications with sufficient margins of 2.68 and 1.35 dB in the n261 band and 3.84 and 4.9 dB in the n260 band, respectively. Notably, the peak and minimum EIRPs of the proposed SGMTS-integrated AiP are measured with only 9 dBm per channel (16 dBm for five channels), which is the power level that the radio frequency integrated circuit can sufficiently supply [18].

V. CONCLUSION

The study proposed a heterogeneous dual-band metasurface empowering proximate ceramic cover for a 5G mmWave smartphone. The minimum distance between the metasurface and AiP and the maximum thickness of the proposed metasurface were determined. We proposed a novel design topology, which groups heterogeneous unit cells into a subarray, to attain dual-band bandwidth control and achieve a wide bandwidth. The metasurfaces integrated with various antenna arrays including the commercial 5G AiP were simulated. In addition, the metasurfaces were embedded in a commercial 5G smartphone with a commercialized AiP to verify its performance. The simulated and measured EIRP cdf results proved the efficiency of the design topology. The proposed metasurface can be applied to various types of target antennas without additional modifications in the antenna design. Moreover, it will enable ceramic covers to be actively used in 5G mmWave smartphones, owing to the numerous design and practical advantages of ceramics.

REFERENCES

[1] J. Seo et al., "Miniaturized dual-band broadside/endfire antenna-in-package for 5G smartphone," *IEEE Trans. Antennas Propag.*, vol. 69, no. 12, pp. 8100–8114, Dec. 2021.

[2] H. Kim and J. Oh, "140-GHz wideband array antenna-in-package using multimode resonance," *IEEE Trans. Antennas Propag.*, vol. 71, no. 3, pp. 2136–2144, Mar. 2023.

[3] M. I. Magray, S.-W. Su, and J.-H. Tarng, "Differential-fed, dual-aperture based, quasi-end-fire 5G mmWave antenna-in-package design," *IEEE Access*, vol. 10, pp. 89091–89100, 2022.

[4] A. Raeesi et al., "A low-profile 2D passive phased-array antenna-in-package for emerging millimeter-wave applications," *IEEE Trans. Antennas Propag.*, vol. 71, no. 1, pp. 1093–1098, Jan. 2023.

[5] M. Xue, W. Wan, Q. Wang, and L. Cao, "Low-profile wideband millimeter-wave antenna-in-package suitable for embedded organic substrate package," *IEEE Trans. Antennas Propag.*, vol. 69, no. 8, pp. 4401–4411, Aug. 2021.

[6] T. H. Lin et al., "Broadband and miniaturized antenna-in-package (AiP) design for 5G applications," *IEEE Antennas Wireless Propag. Lett.*, vol. 19, no. 11, pp. 1963–1967, May 2020.

[7] C.-S. Lee and J.-R. Park, "Multiparametric design of an all-metal, broadband, slant dual-polarized Vivaldi array antenna," *J. Electromagn. Eng. Sci.*, vol. 23, no. 3, pp. 224–232, May 2023.

[8] J. S. Park, J. H. Hong, and K. W. Kim, "Design of 24–40 GHz ultra-wideband circularly polarized monopole antenna with a defected ground plane," *J. Electromagn. Eng. Sci.*, vol. 22, no. 3, pp. 379–385, May 2022.

[9] S. Kamal et al., "A low-profile quasi-loop magneto-electric dipole antenna featuring a wide bandwidth and circular polarization for 5G mmWave device-to-device communication," *J. Electromagn. Eng. Sci.*, vol. 22, no. 4, pp. 459–471, Jul. 2022.

[10] B. Rohrig, "Smartphones: Smart chemistry," *Chem. Matters*, pp. 10–12, Apr./May 2015. [Online]. Available: https://www.acs.org/education/resources/highschool/chemmatters/past-issues/archive-2014-2015/smartphones.html

[11] L. D. Madsen and E. B. Svedberg, *Materials Research for Manufacturing: An Industrial Perspective of Turning Materials Into New Products*. New York, NY, USA: Springer, 2016. [Online]. Available: https://www.sciencedirect.com/science/article/pii/S0376738816314909

[12] J. W. Martin, *Materials for Engineering*. Cambridge, U.K.: Woodhead Publishing, 2006. [Online]. Available: https://books.google.co.kr/books?hl=ko&lr=&id=ALxQAwAAQBAJ&oi=fnd&pg=PP1&dq=Materials+for+Engineering+woodhead&ots=aGZIsUnJQy&sig=a_nh_RMUesVqZjklYmM_jabkJS0&redir_esc=y#v=onepage&q=Materials%20for%20Engineering%20woodhead&f=false

[13] S. Hong, Y. Kim, and J. Oh, "Automobile laminated glass window embedded transmitarray and ray tracing validation for enhanced 5G connectivity," *IEEE Trans. Antennas Propag.*, vol. 70, no. 8, pp. 6671–6682, Aug. 2022.

[14] B. Kim and J. Oh, "Single-glass-layer optically transparent transmitarray with high aperture efficiency and low profile at 5G millimeter-wave band," *IEEE Trans. Antennas Propag.*, vol. 71, no. 11, pp. 9036–9041, Nov. 2023.

[15] R. Z. Jiang et al., "A single-layered wideband and wide-angle transparent metasurface for enhancing the EM-wave transmissions through glass," *IEEE Trans. Antennas Propag.*, vol. 71, no. 8, pp. 6593–6605, Aug. 2023.

[16] A. Bagheri et al., "Enhancing 5G propagation into vehicles and buildings using optically transparent and polarisation insensitive metasurfaces over wide-incidence angles," *Sci. Rep.*, vol. 14, no. 1, p. 6832, 2024.

[17] J. Jung, W. Lee, G. Lee, S. Hong, and J. Oh, "Ultra-thinned metasurface-embedded smartphone antenna-in-package for millimeter-wave 5G/6G coverage enhancement," *IEEE Trans. Antennas Propag.*, vol. 71, no. 10, pp. 7766–7781, Oct. 2023.

[18] S. Kim and S. Nam, "Wideband and ultrathin 2 × 2 dipole array antenna for 5G mmWave applications," *IEEE Antennas Wireless Propag. Lett.*, vol. 21, pp. 2517–2521, 2022.

[19] N. Hussain, M.-J. Jeong, A. Abbas, T.-J. Kim, and N. Kim, "A metasurface-based low-profile wideband circularly polarized patch antenna for 5G millimeter-wave systems," *IEEE Access*, vol. 8, pp. 22127–22135, 2020.

[20] M. A. Sufian, N. Hussain, H. Askari, S. G. Park, K. S. Shin, and N. Kim, "Isolation enhancement of a metasurface-based MIMO antenna using slots and shorting pins," *IEEE Access*, vol. 9, pp. 73533–73543, 2021.

[21] D. Ferreira, R. F. S. Caldeirinha, I. Cuiñas, and T. R. Fernandes, "Square loop and slot frequency selective surfaces study for equivalent circuit model optimization," *IEEE Trans. Antennas Propag.*, vol. 63, no. 9, pp. 3947–3955, Sep. 2015.

[22] *User Equipment (UE) Radio Transmission and Reception; Part 2: Range 2 Standalone (Release 15)*, document TS38.101-2, Version 15.0.0, Jun. 2018.

Byeongjin Kim (Graduate Student Member, IEEE) received the B.S. degree in electrical and computer engineering from Seoul National University, Seoul, South Korea, in 2020, where he is currently pursuing the integrated master's and Ph.D. degrees.

His current research interests include display antenna and antenna-in-package for smartphone, transparent antenna, passive and active transmitarray and reflectarray, and metasurface antenna for 5G millimeter-wave communication systems.

Jaebaek Jung (Graduate Student Member, IEEE) received the B.S. degree in electronic and electrical engineering from Pohang University of Science and Technology (POSTECH), Pohang, South Korea, in 2012. He is currently pursuing the integrated master's and Ph.D. degrees in the Department of Electrical Engineering and Computer Science with Seoul National University, Seoul, South Korea.

His main research interests include mmWave 5G Antenna, 6G Antenna, Metasurface and Antenna in Package.

Sumin Yun received the B.S. and Ph.D. degrees in electrical engineering from Seoul National University, Seoul, South Korea, in 2008 and 2015, respectively.

Since 2015, he has been with Samsung Electronics, Suwon, South Korea. His current research interests include millimeter-wave and ultra-wideband (UWB) antennas, wearable antennas, and microwave active/passive circuits.

Hosaeng Kim (Member, IEEE) received the B.E. degree in school of electronic and electrical engineering from Kyungpook National University, Daegu, South Korea, in 2003, and the M.S. and Ph.D. degrees in electrical engineering from the University of Minnesota, Minneapolis, MN, USA, in 2005 and 2009, respectively.

Since 2009, he has been with Samsung Electronics, Suwon, South Korea, where he is currently the Head of the Advanced Antenna Laboratory, and is involved in a wide range of research and development projects for mobile device antennas. His current research interests include multiband and reconfigurable antennas for 4G/5G handset devices, ultra-wideband (UWB) antenna technology, and millimeter-wave wireless solutions.

Jungsuek Oh (Senior Member, IEEE) received the B.S. and M.S. degrees from Seoul National University, South Korea, in 2002 and 2007, respectively, and the Ph.D. degree from the University of Michigan, Ann Arbor, MI, USA, in 2012.

From 2007 to 2008, he was with Korea Telecom as a Hardware Research Engineer, working on the development of flexible RF devices. In 2012, he was a Post-Doctoral Research Fellow with the Radiation Laboratory, the University of Michigan. From 2013 to 2014, he was a Staff RF Engineer with Samsung Research America, Dallas, TX, USA, working as a Project Leader for the 5G/millimeter-wave antenna system. From 2015 to 2018, he was a Faculty Member with the Department of Electronic Engineering, Inha University, Incheon, South Korea. He is currently an Associate Professor with the School of Electrical and Computer Engineering, Seoul National University. He has published more than 50 technical journal and conference papers. His research interests include mmWave beam focusing/shaping techniques, antenna miniaturization for integrated systems, and radio propagation modeling for indoor scenarios.

Dr. Oh was a TPC member. He was a recipient of the 2011 Rackham Predoctoral Fellowship Award at the University of Michigan. He served as the Session Chair for IEEE AP-S/USNC-URSI and ISAP. He has served as a Technical reviewer for IEEE TRANSACTIONS ON ANTENNAS AND PROPAGATION and IEEE ANTENNA AND WIRELESS PROPAGATION LETTERS.